

Quasiparticle energies and excitonic effects in dense solid hydrogen near metallization

Marc Dvorak,¹ Xiao-Jia Chen,^{2,3} and Zhigang Wu^{1,*}

¹*Department of Physics, Colorado School of Mines, Golden, Colorado 80401, USA*

²*Center for High Pressure Science and Technology Advanced Research, Shanghai 201203, China*

³*Geophysical Laboratory, Carnegie Institution of Washington, Washington, DC 20015, USA*

(Received 10 February 2014; revised manuscript received 13 June 2014; published 3 July 2014)

We investigate the crucial metallization pressure of the *Cmca*-12 phase of solid hydrogen (H) using many-body perturbation theory within the *GW* approximation. We consider the effects of self-consistency, plasmon-pole models, and the vertex correction on the quasiparticle band gap (E_g). Our calculations show that self-consistency leads to an increase in E_g by 0.33 eV over the one-shot G_0W_0 approach. Because of error cancellation between the effects of self-consistency and the vertex correction, the simplest G_0W_0 method underestimates E_g by only 0.16 eV compared with the prediction of the more accurate *GW* Γ approach. Employing the plasmon-pole models underestimates E_g by 0.1–0.2 eV compared to the full-frequency numerical integration results. We thus predict a metallization pressure around 280 GPa, instead of 260 GPa predicted previously. Furthermore, we compute the optical absorption including the electron-hole interaction by solving the Bethe-Salpeter equation (BSE). The resulting absorption spectra demonstrate substantial redshifts and enhancement of absorption peaks compared to the calculated spectra neglecting excitonic effects. We find that the exciton binding energy decreases with increasing pressure from 66 meV at 100 GPa to 12 meV at 200 GPa due to the enhanced electronic screening as solid H approaches metallization. Because optical measurements are so important in identifying the structure of solid H, our BSE results should improve agreement between theory and experiment.

DOI: [10.1103/PhysRevB.90.035103](https://doi.org/10.1103/PhysRevB.90.035103)

PACS number(s): 71.15.-m, 71.20.-b, 71.30.+h, 78.20.-e

I. INTRODUCTION

Hydrogen (H) is both the most abundant and simplest element in the universe. One might incorrectly assume, then, that physicists have a very precise understanding of H at its natural conditions. Unfortunately, the conditions at which much of the H in the universe exists are exceptionally difficult to reproduce in the laboratory. Therefore, the phase diagram and electronic structure of H under extreme conditions remain largely unknown. While the unknown regions of the phase diagram are at high pressures and temperatures that could never naturally occur on earth, they are crucial to astrophysics and planetary science. Moreover, it has been predicted [1–3] that solid H might become superconducting with transition temperature higher than that of any known material, including cuprates. Thus extensive experimental and theoretical efforts continue to tackle the famous hydrogen puzzle [4–10].

A number of unanswered questions regarding solid H remain. There is not yet a broad consensus on the onset of metallization [9] and the stability of phases [4] except for phase I [11,12] because of the notorious difficulties in experimental measurements. In particular, x-ray scattering off of H is extremely low, making the usual crystallographic techniques ineffective. It is also very challenging to accurately measure its optical and excitonic properties under ultrahigh pressures. Theory thus plays a central role in understanding its structural, electronic, and optical properties [7–9,13–16]. Density functional theory (DFT) has been the primary predictive tool in the literature [8,15,16]. However, DFT within the local-density approximation (LDA) or the generalized gradient approximation (GGA) is not expected to precisely predict the phase diagram because of the small

enthalpy differences between competing phases. The neglect of quantum nuclear effects might also lead to sizable errors [13]. Moreover, the onset of metallization estimated by DFT is questionable because the Kohn-Sham (KS) eigenvalues do not correspond to quasiparticle (QP) energies, and using the KS eigenvalues to approximate the QP energies often severely underestimates band gaps (E_g) in a wide range of insulators and semiconductors [17,18]. Nonetheless, the KS band gap can give accurate estimates of the pressure derivative $\partial E_g / \partial P$ [19].

The current state-of-the-art computational approach for QP excitations is many-body perturbation theory within the *GW* approximation [17,18,20]. Recent *GW* calculations [7,21] have predicted an insulator-to-semimetal transition in the *Cmca*-12 phase near 260 GPa. However, the accuracy of the *GW* approximation depends on how such calculations are performed. Plasmon-pole models (PPMs [17,18]) are often employed to replace the frequency-dependent dielectric response function with a model function. In PPMs, certain sum rules are enforced so that explicit evaluation of the dielectric function is limited to zero frequency or up to one more finite frequency. Recent investigations [22,23] suggest that E_g can be quite sensitive to choices in PPM. In practice, the one-shot G_0W_0 with a single iteration is normally carried out. The computationally very demanding self-consistent *GW* calculations are rarely employed, even though self-consistency could also lead to significant changes in E_g [24,25]. More physical results can be obtained if the vertex correction (Γ) is included [26–28], but *GW* Γ calculations are cumbersome and might become intractable.

The major objective of our work is to systematically explore the effects of these various flavors of *GW* calculations on the electronic structure and the metallization pressure of the *Cmca*-12 phase of solid H. Similar to the work that investigated the impact of different density functionals on the electronic structure of solid H [13,14], we study the accuracy

*zhiwu@mines.edu

of a variety of *GW* methods using four common PPMs with different levels of self-consistency and vertex corrections. Here we only consider the *Cmca*-12 phase, which is competitive in phases III and IV. Metallization of solid H is also likely to occur in this phase.

In addition to QP energies, we calculate the optical properties of solid H by solving the Bethe-Salpeter equation (BSE [20,29]) to account for the electron-hole interaction. Theoretical optical-absorption spectra for solid H have been reported previously [7,21], but in these works excitonic effects have been neglected. Because optical measurements are so critical to the identification of the structure of solid H, it is important to compute the optical absorption as accurately as possible. Excitonic effects substantially modify the optical spectrum in semiconductors such as Si, even though the electron-hole interaction in Si is relatively weak [29]. We also compute the exciton binding energy in solid H as a function of pressure, which is an excellent indicator of the strength of the electron-hole interaction.

II. FUNDAMENTAL FORMALISMS

In DFT, the exchange-correlation energy (E_{xc}) is determined by a functional of the total electron density [30]. A set of Schrödinger-like effective single-particle equations based on this principle, the KS equations [31],

$$\left[-\frac{1}{2}\nabla^2 + V_{\text{ext}} + V_{\text{H}} + V_{\text{xc}}\right]\psi_{n\mathbf{k}}^{\text{KS}} = E_{n\mathbf{k}}^{\text{KS}}\psi_{n\mathbf{k}}^{\text{KS}}, \quad (1)$$

can be solved self-consistently to yield the ground-state energy and charge density. Here, V_{xc} is the exchange-correlation potential, the functional derivative of $E_{\text{xc}}[n(\mathbf{r})]$ with respect to density $n(\mathbf{r})$, V_{ext} represents the external potential created by the nuclei and external fields, and V_{H} is the Hartree potential due to classical electrostatic repulsion. KS orbitals $\psi_{n\mathbf{k}}^{\text{KS}}$ and their single-particle eigenvalues $E_{n\mathbf{k}}^{\text{KS}}$ are often interpreted as QP wave functions and energies, though this is formally incorrect.

The actual QP states can be obtained by solving the following QP equation [32],

$$\left[-\frac{1}{2}\nabla^2 + V_{\text{ext}} + V_{\text{H}} + \Sigma(E_{n\mathbf{k}}^{\text{QP}})\right]\psi_{n\mathbf{k}}^{\text{QP}} = E_{n\mathbf{k}}^{\text{QP}}\psi_{n\mathbf{k}}^{\text{QP}}, \quad (2)$$

where $\Sigma(E_{n\mathbf{k}}^{\text{QP}})$ is the self-energy operator. In general, Σ is nonlocal and non-Hermitian, and the imaginary part of its eigenvalues are related to the lifetime of the QP. Casida showed that the exact KS potential is the variationally best local approximation to the exchange-correlation self-energy operator [33]. However, in almost all *GW* calculations, instead of solving the above equation [Eq. (2)], the QP energies are computed by evaluating the following corrections to the KS energies:

$$E_{n\mathbf{k}}^{\text{QP}} = E_{n\mathbf{k}}^{\text{KS}} + \langle \psi_{n\mathbf{k}}^{\text{KS}} | \Sigma(E_{n\mathbf{k}}^{\text{QP}}) - V_{\text{xc}} | \psi_{n\mathbf{k}}^{\text{KS}} \rangle. \quad (3)$$

The frequency dependence of $\Sigma(E)$ is approximated by a linear function in the neighborhood of the KS energy.

Although the self-energy operator can be rigorously derived from many-body theory using a perturbative expansion of the single-particle propagator [32], or Green's function (G), in practice, an approximation to Σ must be made to keep the calculations feasible. The most widely used scheme is the

GW approximation [17,18,20,34],

$$\Sigma = iGW, \quad (4)$$

where G and W are estimated using the KS electronic structure. W is the Coulomb interaction screened by the frequency dependent RPA (random-phase approximation) dielectric function.

Equation (2) describes the single-QP excitations associated with addition or removal of an electron. However, absorption of a photon creates a neutral two-QP excitation that consists of a quasielectron above the Fermi surface and a quasihole below, referred to as an exciton. Accurately describing optical processes, therefore, requires knowledge of the two-QP propagator, whose equation of motion is determined by the Bethe-Salpeter equation (BSE [20,29,35,36]):

$$(E_{c\mathbf{k}}^{\text{QP}} - E_{v\mathbf{k}}^{\text{QP}})A_{v\mathbf{c}\mathbf{k}}^S + \sum_{v'\mathbf{c}'\mathbf{k}'} \langle v\mathbf{c}\mathbf{k} | K^{\text{eh}} | v'\mathbf{c}'\mathbf{k}' \rangle A_{v'\mathbf{c}'\mathbf{k}'}^S = \Omega^S A_{v\mathbf{c}\mathbf{k}}^S. \quad (5)$$

Here $A_{v\mathbf{c}\mathbf{k}}^S$ is the exciton wave function in the basis of QP states, Ω^S is the excitation energy, and K^{eh} is the electron-hole interaction kernel. v and c refer to valence and conduction states, respectively. Optical transitions occur as transitions from the ground state to excitons $A_{v\mathbf{c}\mathbf{k}}^S$, in contrast to transitions from the ground state to independently propagating electrons and holes.

In *GW* calculations, the KS wave functions and eigenvalues are used as a basis to construct the QP Green's function G , while in BSE calculations the KS wave functions are inserted directly into Eq. (5) with QP energy corrections applied to get $E_{n\mathbf{k}}^{\text{QP}}$. The detailed theory and implementation can be found in the literature [18,20,29,32,35,36].

III. RESULTS AND DISCUSSION

A. Crystal and electronic structure

We have reproduced the results of Pickard and Needs [15] for the zero-temperature (ground-state) phase diagram up to 300 GPa using DFT calculations with the PBE-GGA exchange-correlation functional [37] and norm-conserving pseudopotentials [38]. We performed both ground-state structural relaxations and molecular dynamics simulations of finite-temperature annealing to find the global energy minimum. The zero-point lattice vibrations have been shown to have negligible effects on the calculated phase diagram [15]. As shown in Fig. 1, our results suggest that *C2/c* and *Cmca*-12 structures correspond to stable phases III and IV, respectively, with transition pressure around 250 GPa.

In this work, we focus on the *Cmca*-12 structure because the crucial metallization of solid H is likely to occur in this phase. It is also consistent with some experimental data indicating the onset of the insulator-to-metal transition [7]. Figure 2 shows the *Cmca*-12 structure, as originally reported by Pickard and Needs [15]. We construct the 24-atom conventional cell using the symmetry inequivalent atoms described in Ref. [15], and a 12-atom primitive cell is derived from the conventional cell and used throughout. The crystal is a layered structure with ABA stacking, as shown in Fig. 2, and its individual layers are similar to the famous honeycomb structure of graphene [7].

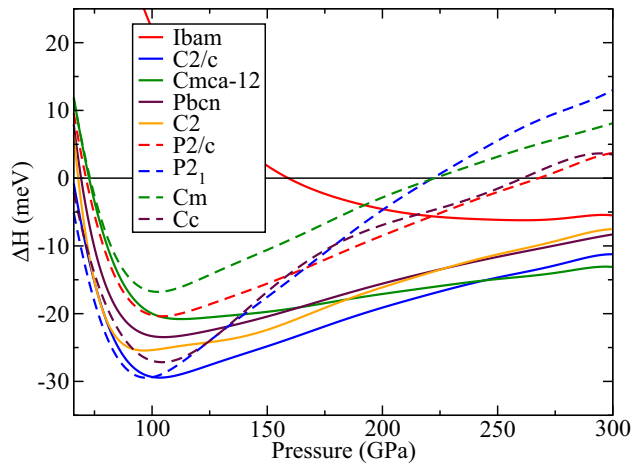


FIG. 1. (Color online) The difference in enthalpy (ΔH) relative to the $Cmca-4$ phase for several candidate structures as a function of pressure.

Next, we examine the reliability of the pseudopotential plus plane-wave method for computing the DFT electronic structure of solid H. Figure 3 shows the electronic band structure of the $Cmca-12$ phase at 250 GPa obtained using three different methods. First, we employ the ABINIT [38–42] package with a very hard norm-conserving pseudopotential ($r_c = 0.2$ a.u.) and a cutoff energy of 120 Ha, and the resulting band structure is plotted in Fig. 3(a). Next, a plane-wave calculation using a much softer pseudopotential ($r_c = 0.9$ a.u.) with a cutoff energy of 30 Ha is carried out, whose results are shown in Fig. 3(b). Finally, we compare the above calculations to the results of a full potential, linearized-augmented-plane-wave (LAPW [43]) calculation implemented in the Elk FP-LAPW code [44] [Fig. 3(c)]. LAPW calculations use a muffin-tin radius of 0.68 a.u. and an rG_{\max} value of 7.0. These three band structures agree very well with each other, and are also in very good agreement with previous work [14,16]. At any pressure from 100 to 250 GPa, the deviation in band gaps, which are between the halfway point of the Γ - Y segment (valence-band maximum,

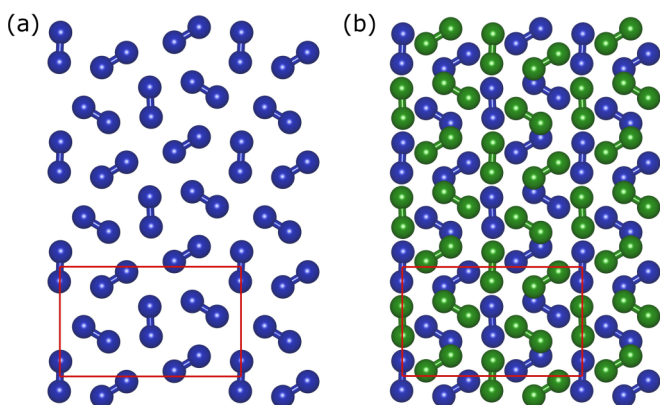


FIG. 2. (Color online) The $Cmca-12$ crystal structure. (a) A single layer and (b) ABA stacking, with the conventional unit cell shown in red. Blue and green solid spheres represent protons on A and B layers, respectively.

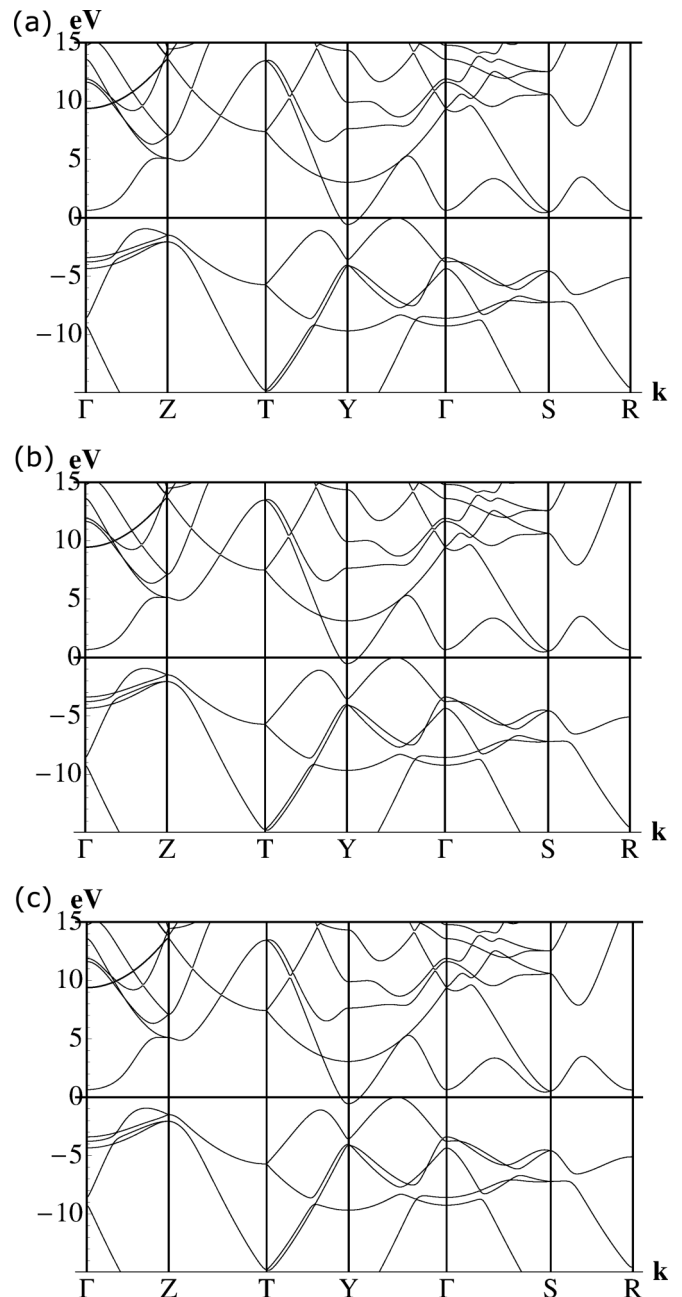


FIG. 3. Calculated electronic band structures of the $Cmca-12$ phase at 250 GPa based on DFT, using (a) a very hard norm-conserving pseudopotential and plane waves, (b) a much softer pseudopotential with plane waves, and (c) the all-electron full potential LAPW method. Overlaps between the VBM and CBM are 0.57, 0.53, and 0.47 eV in panels (a), (b), and (c), respectively.

VBM) and the Y -point (conduction-band minimum, CBM), due to the three different methods is less than 0.1 eV. At high pressures, the electronic structure is semimetallic, and we compare the overlap between the VBM and CBM at the same points. With this excellent agreement, we assert that we can use the relatively soft pseudopotential with plane waves in the present investigation of electronic structure up to 250 GPa.

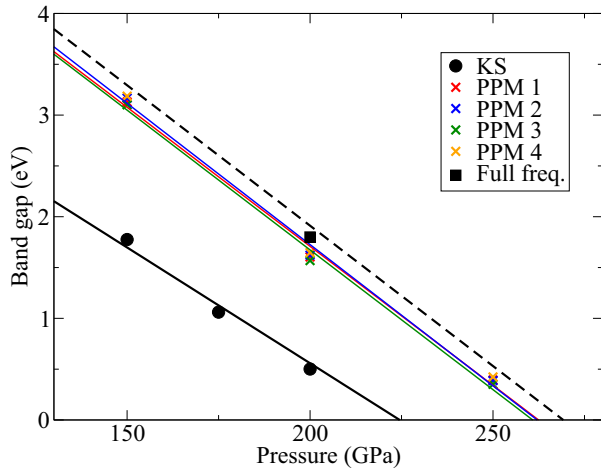


FIG. 4. (Color online) Band gap of *Cmca*-12 solid hydrogen as a function of pressure in the G_0W_0 approximation using 4 PPMs (described in text) and the numerical full-frequency dependent screening. Solid lines are linear fits to their respective data points. The dashed line is a rigid shift of the fit to the PPM 2 data, shifted by the difference between the full-frequency calculation (square data point) and the PPM 2 calculation (red \times) at 200 GPa. KS indicates the Kohn-Sham band gap.

B. Quasiparticle energies

All GW calculations in this work are performed on an unshifted $8 \times 8 \times 8$ \mathbf{k} -point grid, yielding 105 irreducible \mathbf{k} points. The dynamical screening (W) is calculated on the same grid of \mathbf{q} points. An unshifted $8 \times 8 \times 8$ grid has the advantage of containing the VBM at the reciprocal-lattice coordinates $(\frac{3}{4}, \frac{1}{4}, 0)$ on the Γ - Y segment and the CBM at the Y point $(\frac{1}{2}, \frac{1}{2}, 0)$. Therefore, no \mathbf{k} -point interpolation is required to compute the fundamental band gap. Initial DFT calculations use the PBE-GGA exchange-correlation functional. The screening is evaluated with a cutoff energy of 15 Ha with the sum over states performed up to 200 bands. The correlation part of Σ is calculated up to a cutoff of 15 Ha, the exchange is calculated with a cutoff of 30 Ha, and 150 total bands are used in the self-energy summations. We use the ABINIT package and cross check in certain cases with QUANTUM ESPRESSO [45] and BerkeleyGW [46].

We start by studying the effect of the PPM in the one-shot G_0W_0 calculations. We compare E_g calculated with four common PPMs constructed by (1) Godby and Needs [47], (2) Hybertsen and Louie [17], (3) von der Linden and Horsh [48], and (4) Farid and Engel [49]. Brief details of the PPMs are in the Appendix. As summarized in Fig. 4 and Table I, these

TABLE I. Calculated band gaps (E_g in eV) for *Cmca*-12 solid H as a function of pressure (GPa) using the G_0W_0 method with different plasmon-pole models. KS indicates the Kohn-Sham band gap.

Pressure	KS	PPM 1	PPM 2	PPM 3	PPM 4
150	1.78	3.13	3.17	3.10	3.19
200	0.50	1.60	1.62	1.57	1.65
250		0.40	0.39	0.35	0.42

four PPMs agree well with each other on the magnitude of the band gap, with the largest difference among them being merely 0.09 eV. The Hybertsen-Louie PPM was cross checked by QUANTUM ESPRESSO/BerkeleyGW. The difference between the two packages is less than 8 meV.

The QP corrections to the KS eigenvalues decrease with pressure, or, equivalently, the KS energies better approximate the QP energies as pressure increases. Despite this small shift in corrections, the derivative $\partial E_g / \partial P$ predicted by the KS eigenvalues still agrees well with GW results. A linear fitting to the G_0W_0 band gap as a function of pressure is nearly a rigid shift of the KS fit. G_0W_0 predicts a metallization pressure of 260 GPa, in comparison with 225 GPa predicted by KS-DFT. Our estimate is in good agreement with previous work [21]. Note that the metallization here is an insulator-to-semimetal transition (Fig. 3), since there is an indirect overlap of valence and conduction bands above the transition pressure.

Comparing the four PPMs to each other does not actually assess their accuracy, however, since they may all have similar errors compared to the full-frequency dependent dielectric function. To test this, we compute G_0W_0 corrections using the real-axis integration method implemented in BerkeleyGW [46]. In this highly expensive technique, the screening is evaluated on a grid of frequencies, and the self-energy is computed as a numerical integral along the real frequency axis. We perform the frequency dependent screening calculation only at 200 GPa and found a band gap of 1.80 eV, compared with the largest band gap of 1.64 eV computed using the Hybertsen-Louie PPM. All of the PPMs, then, tend to underestimate the band gap of solid H compared to the frequency dependent screening. Because the pressure derivative of the band gap is relatively constant across all methods, we extrapolate the band gap calculated with full frequency dependence to higher pressures from this single data point. A small increase of 0.16 eV in E_g corresponds to an upward shift in metallization pressure of less than 10 GPa, as indicated in Fig. 4, which we consider to be an acceptable error due to the PPM.

Next, we test the effect of self-consistency on band gap. ABINIT is able to perform self-consistent GW calculations on two levels: eigenvalues only or eigenvalues with eigenvectors. In the case of eigenvalue self-consistency, the self-energy is constructed in the basis of KS eigenstates with the matrix elements at each \mathbf{k} point:

$$H_{(i+1)}^{\text{QP}}(E) = E_{n\mathbf{k},(i)}^{\text{QP}} \delta_{n,m} + \langle \psi_{n\mathbf{k}}^{\text{KS}} | \Sigma_{(i)}(E) - V_{\text{xc}} | \psi_{m\mathbf{k}}^{\text{KS}} \rangle. \quad (6)$$

Here i represents the i th iteration, with $i = 0$ equal to the KS energies. The eigenvalues of this Hamiltonian are new QP energies that, in general, are not equal to the perturbative energies of Eq. (3). In the case of self-consistency on both eigenvalues and eigenvectors, each iteration finds new QP energies and wave functions that are used in the next iteration to update $H_{(i)}^{\text{QP}}(E)$:

$$H_{(i+1)}^{\text{QP}}(E) = E_{n\mathbf{k},(i)}^{\text{QP}} \delta_{n,m} + \langle \psi_{n\mathbf{k},(i)}^{\text{QP}} | \Sigma_{(i)}(E) - V_{\text{xc}} | \psi_{m\mathbf{k},(i)}^{\text{QP}} \rangle. \quad (7)$$

The first iteration of either Eq. (6) or Eq. (7) is a G_0W_0 calculation including the off-diagonal elements of the self-energy. Before considering the effect of self-consistency, we

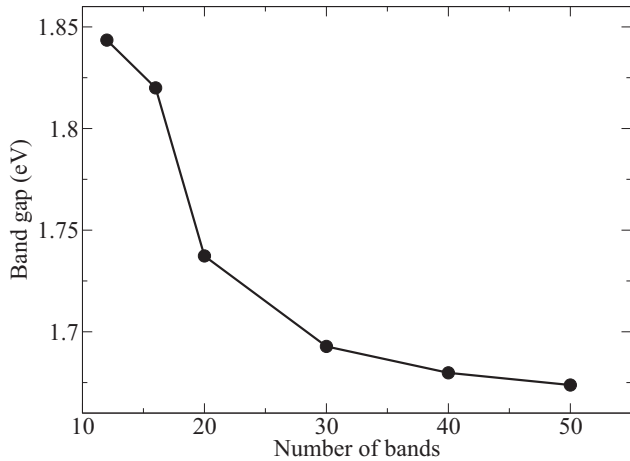


FIG. 5. G_0W_0 band gap of *Cmca*-12 solid hydrogen including off-diagonal matrix elements at 200 GPa, using the PPM of Godby and Needs.

focus on the role of the off-diagonal matrix elements. Figure 5 shows the convergence of the band gap with respect to the dimension of the self-energy matrix. Extrapolating Fig. 5 to a complete basis (∞ number of bands), we estimate that constructing the self-energy with 50 bands gives an error of less than 7 meV in E_g . With 50 bands, $E_g = 1.67$ eV, very close to the perturbative G_0W_0 value of 1.60 eV. However, using too few bands gives noticeable errors, e.g., E_g of 1.84 eV with only 12 bands, an error of 0.17 eV. Fortunately, the converged band gap with off-diagonal matrix elements included is very close to the perturbative value using diagonal matrix elements only. Thus, the effect of the off-diagonal matrix elements on metallization pressure is negligible.

We perform both eigenvalue only and eigenvalue plus eigenvector self-consistent calculations using two PPMs constructed by (1) Godby and Needs and (2) Hybertsen and Louie. Our self-consistent calculations include the off-diagonal matrix elements of the self-energy, and we update both G and W iteratively in $H_{(i)}^{QP}(E)$. Such calculations are extremely demanding, and we can only use 16 bands, even though Fig. 5 indicates that 50 bands are necessary to reach convergence with respect to the off-diagonal matrix elements. We remedy the small incomplete basis error by applying a -0.15 eV correction to our calculations using 16 bands. The -0.15 eV correction is obtained from G_0W_0 calculations (Fig. 5) as the difference in E_g between calculations with 16 and 50 bands, which assumes that the corrections to the QP energies due to an improved basis are independent of self-consistency.

Table II summarizes the band gap computed with these two versions of self-consistency, as well as the non-self-consistent G_0W_0 for reference. For self-consistent calculations, the difference between PPMs is approximately 0.04 eV, in close agreement with the non-self-consistent G_0W_0 results. Eigenvalue self-consistency leads to an increase of ~ 0.1 eV in band gap. This increase agrees well with the work of Shishkin and Kresse, who found that G_0W_0 systematically underestimates band gaps compared with eigenvalue self-consistent GW [24]. Including eigenvector self-consistency further enhances band gaps by roughly 0.22 eV, suggesting that there are nontrivial

TABLE II. Calculated band gaps (E_g in eV) for *Cmca*-12 solid H at 200 GPa using the self-consistent GW method. Y (N) indicates self-consistency (no self-consistency) on eigenvalues or eigenvectors. All calculations include the off-diagonal elements of the self-energy up to 16 bands. For the non-self-consistent calculation (row 1, G_0W_0), the extrapolated gap (E_g^{extrap}) is the actual value with 50 bands as shown in Fig. 5. For the remaining rows, E_g^{extrap} are obtained by applying the same shift of -0.15 eV as that in the first row.

Eigenvalue	Eigenvector	PPM	E_g	E_g^{extrap}
N	N	1	1.82	1.67
Y	N	1	1.92	1.77
Y	N	2	1.96	1.81
Y	Y	1	2.15	2.00
Y	Y	2	2.18	2.03

deviations between the starting KS wave functions and the true QP wave functions obtained by diagonalizing the self-energy.

Depending on the choice of PPM and self-consistency, our calculated E_g of solid H at 200 GPa falls within a range of about 0.36 eV. Based on Fig. 4, 0.36 eV corresponds to an upward shift of ~ 20 GPa in the metallization pressure. Up to this point, our most physical calculations are the eigenvalue plus eigenvector self-consistent calculations, for which results are shown in the bottom two rows of Table II. Those are, in principle, our most accurate predictions based on the GW approximation. We note that our zero-temperature electronic structure calculations ignore the effects of the electron-phonon interaction, however, which could renormalize the band gap and shift the metallization pressure accordingly.

Because of the noticeable differences between the two types of self-consistency in Table II, we now elaborate on the quality of the starting KS wave functions. Figure 6 shows the difference between the GW QP density and the KS charge density, $n^{\text{diff}}(\mathbf{r}) = n^{\text{QP}}(\mathbf{r}) - n^{\text{KS}}(\mathbf{r})$. The majority of the difference is localized on the H-H bonds, which is indicative of the intrinsic problem of using KS wave functions to describe QP wave functions.

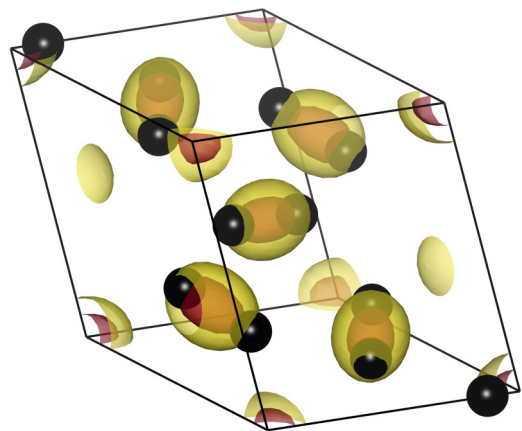


FIG. 6. (Color online) Difference in eigenvector self-consistent GW (PPM of Hybertsen and Louie) and DFT charge densities of solid H at 200 GPa. Red and yellow indicate high and low isosurface values, and the black spheres represent protons.

We further quantify the difference in charge densities by integrating $|n^{\text{diff}}(\mathbf{r})|$ over one primitive cell, and we find that roughly 0.13 occupied states per cell are deviated from the DFT charge density. For comparison, we repeat the calculation for Si at ambient conditions and find a deviation of only 0.02 occupied states per cell. Normalized by the total charge in their respective cells for comparison, *Cmca*-12 hydrogen has an average of 0.011 charge variation between *GW* and DFT per electron, compared to 0.0025 for Si. This is certainly not a definitive conclusion on the quality of individual KS wave functions in solid H, but it does point to a qualitative difference between solid H and Si. Given the band-gap values in Table II and the distribution displayed in Fig. 6, we conclude that there are meaningful deviations between KS states and *GW* QP wave functions in *Cmca*-12 hydrogen.

Finally, we include the vertex correction to calculate QP energies in the *GW* Γ approximation. In the ordinary *GW* approximation, the vertex function is $\Gamma(1,2;3) = \delta(1,2)\delta(1,3)$, which results in the self-energy Σ being a product of *G* and *W*. The neglect of the features in Γ in the *GW* approximation makes the calculations tractable, but its reliability compared to *GW* Γ has only been partly investigated [27,28].

The self-energy in Hedin's equations is [34]

$$\Sigma(1,2) = i \int d(3,4)W(1^+,3)G(1,4)\Gamma(4,2;3), \quad (8)$$

where each number is a set of position, spin, and time coordinates. In the ABINIT implementation [26] of *GW* Γ , the screened interaction *W* of *GW* is replaced by an effective interaction \tilde{W} . Assuming the starting self-energy Σ is the DFT exchange-correlation potential, one can derive the electron-test-charge dielectric function and \tilde{W} :

$$\tilde{W} = v[1 - \chi^0(v + K_{xc})]^{-1}. \quad (9)$$

Here *v* is the bare Coulomb interaction, χ^0 is the single-particle polarizability, and the exchange-correlation kernel K_{xc} is the functional derivative of V_{xc} with respect to density,

$$K_{xc} = \frac{\delta V_{xc}(1)}{\delta n(2)}, \quad (10)$$

contributing an effective exchange-correlation potential to the interaction. In contrast, *W* contains only the screened Coulomb interaction.

Table III shows band gaps calculated in the *GW* Γ approximation. First, the perturbative $G_0W_0\Gamma$ gap, i.e., only

TABLE III. Calculated band gaps (E_g in eV) for *Cmca*-12 solid H at 200 GPa using the *GW* Γ method. Y (N) indicates self-consistency (no self-consistency) on eigenvalues or eigenvectors and whether or not the off-diagonal matrix elements (denoted by ‘‘Off-Diag’’) are considered. In all the off-diagonal calculations we used 16 bands, and again the extrapolated gaps (E_g^{extrap}) are obtained by applying the same shift of -0.15 eV as in Table II.

Eigenvalue	Eigenvector	Off-Diag	E_g	E_g^{extrap}
N	N	N	1.62	
Y	N	Y	1.84	1.69
Y	N	Y	1.87	1.72
Y	Y	Y	1.95	1.80

the diagonal matrix elements of Σ , are considered, agrees well with the corresponding G_0W_0 calculation. Including the vertex function Γ increases the band gap by only 0.01 eV. Including the off-diagonal matrix elements of Σ in the $G_0W_0\Gamma$ calculation also gives a result very close to that of its G_0W_0 analog with merely a 0.02 eV increase in E_g . Interestingly, including the vertex function in self-consistent calculations predicts smaller band gaps than those obtained using self-consistent *GW*. Specifically, eigenvalue self-consistent *GW* Γ predicts a band gap 0.05 eV smaller than the corresponding *GW*. Including eigenvector self-consistency with the vertex function predicts a 0.2 eV reduction in E_g compared to self-consistent *GW*.

Therefore, the band gap increase associated with self-consistency is largely compensated by including Γ . Due to this error cancellation between self-consistency and the vertex correction, the most accurate—but tremendously demanding—self-consistent *GW* Γ calculation predicts a band gap (1.80 eV) only 0.16 eV higher than $E_g = 1.64$ eV calculated with the simplest perturbative G_0W_0 method. This small difference in E_g increases the metallization pressure of solid hydrogen by around 10 GPa. Considering the PPM used in place of the frequency dependent dielectric function, our calculations point to a metallization pressure around 280 GPa.

C. Optical properties

We compute optical properties using KS wave functions computed with the QUANTUM ESPRESSO package [45] that are fed into the BerkeleyGW [46] code to solve the Bethe-Salpeter equation for correlated electron-hole states in the Tamm-Dancoff approximation. Optical properties typically require very dense \mathbf{k} -point sampling to reach convergence. The primary advantage of BerkeleyGW is its unique interpolation scheme that allows the electron-hole kernel (K^{eh}) to be accurately interpolated from a sparse \mathbf{k} -point grid onto a denser grid [29,46]. We compute K^{eh} on an $8 \times 8 \times 8$ \mathbf{k} -grid and interpolate the interaction onto a $24 \times 24 \times 24$ grid. The kernel is calculated for all six occupied bands and the 12 lowest unoccupied bands, then interpolated onto all occupied bands and the six lowest unoccupied bands. The extra states on the sparse grid improve the quality of the interpolation. The dielectric function is obtained using the iterative Haydock recursion method that avoids diagonalizing the entire BSE Hamiltonian [50]. Exciton binding energies (E_g) are calculated by interpolating the kernel onto a dense grid of \mathbf{k} points surrounding the optical gap and diagonalizing the two-QP Hamiltonian [51–53].

Figure 7 shows the imaginary part of the dielectric function (ϵ_2) of *Cmca*-12 hydrogen at three different pressures. G_0W_0 corrections with the Hybertsen-Louie PPM are applied to correct QP energies, and the optical gap is near the \mathbf{k} point $(-3/8, 3/8, 0)$. The imaginary part of the dielectric function ϵ_2 is computed as

$$\epsilon_2(\omega) = \frac{16\pi^2 e^2}{\omega^2} \sum_s |\mathbf{e} \cdot \langle 0 | \mathbf{v} | S \rangle|^2 \delta(\omega - \Omega^S), \quad (11)$$

for exciton states $|S\rangle$, exciton energies Ω^S , and light polarization vector \mathbf{e} . Here \mathbf{v} is the single-particle velocity

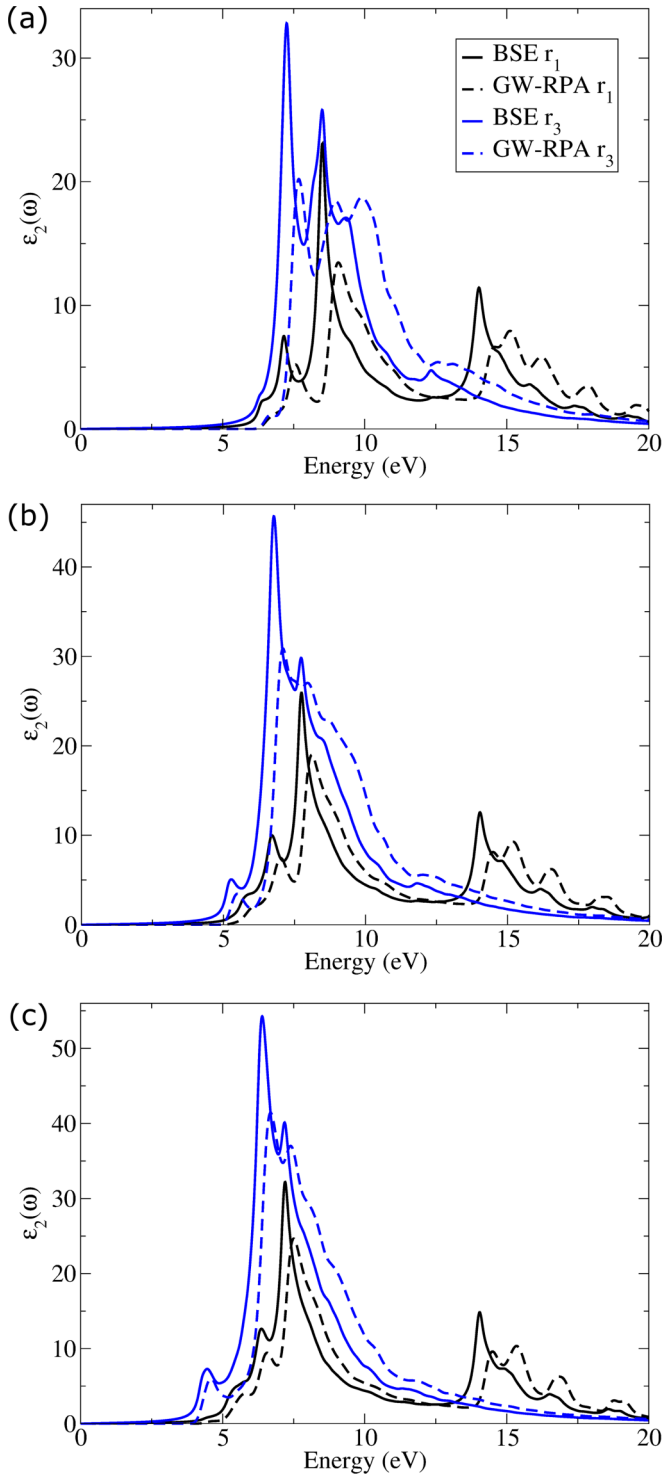


FIG. 7. (Color online) Imaginary part of the dielectric function for *Cmca*-12 hydrogen at (a) 100, (b) 150, and (c) 200 GPa for polarizations along the crystalline axes \mathbf{r}_1 and \mathbf{r}_3 with (BSE) and without (GW-RPA) the electron-hole interaction. A thermal broadening of 0.15 eV is applied.

operator. In general, the electron-hole interaction enhances absorption peaks and induces a redshift in the absorption spectrum of insulators compared to the *GW*-RPA (random-phase approximation) spectrum [51,52,54]. Our work shows

TABLE IV. Exciton binding energy (E_b in meV) as a function of pressure (in GPa) in *Cmca*-12 solid hydrogen. Here E_g^* is the optical gap calculated with the BSE (in eV), and ϵ is the static dielectric constant.

Pressure	E_g^*	ϵ	E_b
100	6.39	7.40	66
150	5.17	10.27	29
200	4.22	13.40	12

that this is also true in the present calculation for solid H. While these changes are expected and perhaps unremarkable, they are not necessarily unimportant. The shifts between the BSE and *GW*-RPA spectra are on the order of 0.5 eV, which could be comparable to shifts in absorption peaks between competing phases. Comparison of theoretical absorption spectra without excitonic effects to experiment, then, could give poor agreement even if the correct phase is identified.

The shifts between the BSE and *GW*-RPA spectra cannot be attributed entirely to electron-hole binding. Exciton binding energies are, in general, much smaller, on the order or tens of meV. The shift in the absorption is due to a coherent superposition of the optical matrix elements between electron-hole pairs that make up the matrix element in Eq. (11) at low energies [29]. As pressure increases, there is an enhancement of the first absorption peak near 5 eV, as well as a decrease in the shoulder near 9 eV and the peak near 7.5 eV. The primary absorption peak remains relatively unchanged with pressure, except for the obvious redshift with band-gap closure. There are also pronounced differences in the dielectric function for light polarized along the crystal vectors \mathbf{r}_1 and \mathbf{r}_3 due to the planar structure of *Cmca*-12.

We also compute exciton binding energies (E_b) as the difference between the direct quasiparticle gap (E_g^{direct}) and the lowest exciton energy, or optical gap (E_g^*), $E_b = E_g^{\text{direct}} - E_g^*$, as summarized in Table IV. In *Cmca*-12 hydrogen, excitons are of the weakly bound Wannier-Mott type, as is commonly seen in many covalently bonded semiconductors. Furthermore, E_b on the order of tens of meV is similar to those in common semiconductors [51–53]. As pressure increases and the band gap reduces, the static dielectric constant ϵ increases and E_b drops due to enhanced electronic screening. This behavior is contrary to more familiar materials like the III-V semiconductors, which show a decrease in dielectric constant with increasing pressure [55]. For the lowest energy $1s$ -like exciton, there are no appreciable amplitudes of electron-hole pairs contributing to the exciton beyond the two highest (lowest) valence (conduction) bands. We expect the neglect of the coupling block in the BSE (the Tamm-Dancoff approximation) between electron-hole pairs and antipairs to be acceptable. The coupling is expected to be more important as confinement is increased and dimensionality is reduced from bulk materials [56]. Our conclusion is that solid hydrogen has no dramatic excitonic effects, but their impact on the theoretical absorption spectrum is important for agreement with experiment.

IV. CONCLUSION

An outstanding problem in the GW approach is that its accuracy in predicting band gaps depends on how the calculation is carried out. The simplest one-shot G_0W_0 works perfectly for simple semiconductors such as Si and C, however it underestimates E_g in materials with more localized valence electrons, such as ZnO. The self-consistent GW calculation tends to overestimate E_g for simple semiconductors, though it predicts better E_g for oxides than G_0W_0 [24]. In this work we carefully examined the effects of the plasmon-pole models, off-diagonal matrix elements of self-energy, self-consistency in eigenvalues and eigenvectors, and the vertex correction on the band gap of $Cmca$ -12 solid hydrogen. Our results show a variation as large as ~ 0.4 eV in E_g for solid H at 200 GPa when comparing the G_0W_0 gap (1.64 eV) with that of self-consistent GW (2.03 eV). Including the vertex correction reduces E_g to 1.80 eV, demonstrating that the error cancellation between self-consistency and the vertex correction makes the efficient G_0W_0 method unexpectedly accurate. Thus, the present results also help explain the serendipitous success of G_0W_0 in predicting band gaps in insulators despite its known conceptual shortcomings. A ~ 0.2 eV increase in band gap for $Cmca$ -12 hydrogen by consideration of the vertex correction, self-consistency, and off-diagonal matrix elements of the self-energy corresponds to a ~ 10 GPa shift in metallization pressure from 260 to 270 GPa. If the error due to using a PPM is also corrected, we expect the transition pressure to be around 280 GPa.

Therefore, the total error of the $G_0W_0 + \text{PPM}$ approach is about 20 GPa in transition pressure (0.3–0.4 eV in E_g) for solid H in phase III. Since the difference in transition pressures between the G_0W_0 and DFT results is only 35 GPa, this rather noticeable error due to various approximations involved in GW calculations should pose a caution to the reliability of the widespread $G_0W_0 + \text{HL PPM}$ method for solid hydrogen and similar electronic systems.

The metallization of solid hydrogen at low temperature might occur in another more stable crystal structure than $Cmca$ -12, which has not been confirmed experimentally. That possibility is still a matter of debate. We believe that the QP electronic structure and the metallization pressure for any new crystal structure can still be computed reliably with perturbative G_0W_0 using a plasmon-pole model. The work of Lebegue *et al.* [21] has shown that differences in metallization pressure between phases is typically larger than the 20 GPa error we attribute to G_0W_0 . Because of the similar chemical environment between competing crystal structures, we expect our conclusions regarding the accuracy of G_0W_0 to hold across phases. Lebegue's G_0W_0 investigation of metallization for several phases of solid H could reasonably be extended to study several additional crystal structures for possibly better experimental verification.

Previous work has shown excellent agreement in optical properties of semiconductors and insulators between theoretical results obtained with the BSE and experimental results [29,51,53,54]. Therefore, we expect our present BSE calculations on absorption spectra to help identify crystal structures of solid H using optical processes in addition to x-ray scattering. We find that the electron-hole interaction in

$Cmca$ -12 is relatively weak with E_b decreasing from 66 meV at 100 GPa to 12 meV at 200 GPa, but the excitonic effects still substantially modify the optical absorption compared to the GW -RPA results. Similar to the prediction of metallization pressures, optical-absorption spectra including excitonic effects for several competitive crystal structures could be calculated to provide a useful comparison to experiment.

ACKNOWLEDGMENTS

This work was supported by US DOE Early Career Award (Grant No. DE-SC0006433) and the startup funding from Colorado School of Mines (CSM). Computations were carried out at the Golden Energy Computing Organization at CSM and the National Energy Research Scientific Computing Center (NERSC). The authors thank M. Lusk and D. Wood for insightful discussions.

APPENDIX: PLASMON-POLE MODELS

In the plasmon-pole models of Godby/Needs and Hybertsen/Louie, [17,47,57] the real and imaginary parts of the dielectric function take the form

$$\begin{aligned} \text{Re}[\epsilon_{\mathbf{G}\mathbf{G}'}^{-1}(\mathbf{q}, \omega)] &= \delta_{\mathbf{G}\mathbf{G}'} + \frac{\Omega_{\mathbf{G}\mathbf{G}'}^2(\mathbf{q})}{\omega^2 - \tilde{\omega}_{\mathbf{G}\mathbf{G}'}^2(\mathbf{q})}, \\ \text{Im}[\epsilon_{\mathbf{G}\mathbf{G}'}^{-1}(\mathbf{q}, \omega)] &= A_{\mathbf{G}\mathbf{G}'}(\mathbf{q})\delta\{\omega - \tilde{\omega}_{\mathbf{G}\mathbf{G}'}(\mathbf{q})\} \\ &\quad - \delta\{\omega + \tilde{\omega}_{\mathbf{G}\mathbf{G}'}(\mathbf{q})\}. \end{aligned} \quad (\text{A1})$$

$\tilde{\omega}_{\mathbf{G}\mathbf{G}'}(\mathbf{q})$ is the plasmon frequency with effective amplitude $A_{\mathbf{G}\mathbf{G}'}(\mathbf{q})$, and $\Omega_{\mathbf{G}\mathbf{G}'}^2(\mathbf{q}) = -A_{\mathbf{G}\mathbf{G}'}(\mathbf{q})\tilde{\omega}_{\mathbf{G}\mathbf{G}'}^2(\mathbf{q})$. In the GN case, the plasmon-pole parameters are chosen to reproduce the behavior of the actual $\epsilon_{\mathbf{G}\mathbf{G}'}^{-1}(\mathbf{q}, \omega)$ in the static limit ($\omega = 0$) and at one finite imaginary frequency. For the HL PPM, a generalized f -sum rule is enforced to determine the parameters.

In the PPM of von der Linden and Horsh [48], the dielectric function is expressed as

$$\epsilon_{\mathbf{G}\mathbf{G}'}^{-1}(\mathbf{q}; 0) = \delta_{\mathbf{G}\mathbf{G}'} + \sum_{i=1}^{\infty} U_{\mathbf{q},i}(\mathbf{G})[\epsilon_i^{-1}(\mathbf{q}) - 1]U_{\mathbf{q},i}^*(\mathbf{G}'), \quad (\text{A2})$$

where U is the matrix formed by the eigenvectors of the inverse dielectric function. The remaining quantities are determined by

$$\begin{aligned} \epsilon_i^{-1}(\mathbf{q}, \omega) - 1 &= \frac{z_i(\mathbf{q})}{\omega^2 - [\omega_i(\mathbf{q})^2 - i\delta]^2}, \\ z_i(\mathbf{q}) &= \frac{\omega_{pl}^2}{\rho(0)} \sum_{\mathbf{G}, \mathbf{G}'} U_{\mathbf{q},i}^*(\mathbf{G}) \frac{(\mathbf{q} + \mathbf{G}) \cdot (\mathbf{q} + \mathbf{G}')}{\|\mathbf{q} + \mathbf{G}\| \|\mathbf{q} + \mathbf{G}'\|} \\ &\quad \times \rho(\mathbf{G} - \mathbf{G}') U_{\mathbf{q},i}(\mathbf{G}'), \\ \omega_i^2(\mathbf{q}) &= \frac{z_i(\mathbf{q})}{1 - \epsilon_i^{-1}(\mathbf{q})}; \end{aligned} \quad (\text{A3})$$

ω_{pl} is the free-electron plasma frequency $\omega_{pl}^2 = 4\pi\rho(0)$. The last two relationships are determined by the Johnson sum rule.

The PPM of Farid and Engel [49] is obtained by diagonalizing

$$\tilde{\chi}(\mathbf{q}; \omega) \equiv [\epsilon^2 M^{-1}(\mathbf{q}) + \chi^{-1}(\mathbf{q}; 0)]^{-1}, \quad (\text{A4})$$

where $M_{\mathbf{G}\mathbf{G}'}(\mathbf{q}) \equiv -(2/\pi)\chi_{\mathbf{G}\mathbf{G}'}^{(1)}(\mathbf{q})$ and $\chi_{\mathbf{G}\mathbf{G}'}^{(1)}(\mathbf{q})$ is the first energy moment of the polarizability. $\tilde{\chi}(\mathbf{q}; \omega)$ is constructed to match $\chi(\mathbf{q}; \omega)$ at $\omega = 0$ and has the correct asymptotic behavior as $|\omega| \rightarrow \infty$.

-
- [1] E. Wigner and H. B. Huntington, *J. Chem. Phys.* **3**, 764 (1935).
- [2] N. W. Ashcroft, *Phys. Rev. Lett.* **21**, 1748 (1968).
- [3] P. Cudazzo, G. Profeta, A. Sanna, A. Floris, A. Continenza, S. Massidda, and E. K. U. Gross, *Phys. Rev. Lett.* **100**, 257001 (2008).
- [4] H.-k. Mao and R. J. Hemley, *Rev. Mod. Phys.* **66**, 671 (1994).
- [5] J. M. McMahon, M. A. Morales, C. Pierleoni, and D. M. Ceperley, *Rev. Mod. Phys.* **84**, 1607 (2012).
- [6] A. F. Goncharov, J. S. Tse, H. Wang, J. Yang, V. V. Struzhkin, R. T. Howie, and E. Gregoryanz, *Phys. Rev. B* **87**, 024101 (2013).
- [7] R. E. Cohen, I. I. Naumov, and R. J. Hemley, *Proc. Natl. Acad. Sci. USA* **110**, 13757 (2013).
- [8] S. A. Bonev, E. Schegler, T. Ogitsu, and G. Galli, *Nature (London)* **431**, 669 (2004).
- [9] M. I. Eremets and I. A. Troyan, *Nat. Mater.* **10**, 927 (2011).
- [10] J. Chen, X.-Z. Li, Q. Zhang, M. I. J. Probert, C. J. Pickard, R. J. Needs, A. Michaelides, and E. Wang, *Nat. Commun.* **4**, 2064 (2013).
- [11] P. Loubeyre, R. LeToullec, D. Hausermann, M. Hanfland, R. J. Hemley, H. K. Mao, and L. W. Finger, *Nature (London)* **383**, 702 (1996).
- [12] I. Goncharenko and P. Loubeyre, *Nature (London)* **435**, 1206 (2005).
- [13] M. A. Morales, J. M. McMahon, C. Pierleoni, and D. M. Ceperley, *Phys. Rev. B* **87**, 184107 (2013).
- [14] S. Azadi and W. M. C. Foulkes, *Phys. Rev. B* **88**, 014115 (2013).
- [15] C. J. Pickard and R. J. Needs, *Nat. Phys.* **3**, 473 (2007).
- [16] C. J. Pickard, M. Martinez-Canales, and R. J. Needs, *Phys. Rev. B* **85**, 214114 (2012).
- [17] M. S. Hybertsen and S. G. Louie, *Phys. Rev. B* **34**, 5390 (1986).
- [18] W. G. Aulbur, L. J ansson, and J. W. Wilkins, *Quasiparticle Calculations in Solids*, edited by H. Ehrenreich and F. Spaepen, Solid State Physics Vol. 54 (Academic, Amsterdam, 1999), pp. 1–218.
- [19] S. B. Trickey, A. K. Ray, and J. P. Worth, *Phys. Status Solidi B* **106**, 613 (1981).
- [20] G. Onida, L. Reining, and A. Rubio, *Rev. Mod. Phys.* **74**, 601 (2002).
- [21] S. Leb g ue, C. M. Araujo, D. Y. Kim, M. Ramzan, H.-k. Mao, and R. Ahuja, *Proc. Natl. Acad. Sci. USA* **109**, 9766 (2012).
- [22] M. Stankovski, G. Antonius, D. Waroquiers, A. Miglio, H. Dixit, K. Sankaran, M. Giantomassi, X. Gonze, M. C t e, and G.-M. Rignanese, *Phys. Rev. B* **84**, 241201 (2011).
- [23] P. Larson, M. Dvorak, and Z. Wu, *Phys. Rev. B* **88**, 125205 (2013).
- [24] M. Shishkin and G. Kresse, *Phys. Rev. B* **75**, 235102 (2007).
- [25] F. Bruneval, N. Vast, and L. Reining, *Phys. Rev. B* **74**, 045102 (2006).
- [26] R. Del Sole, L. Reining, and R. W. Godby, *Phys. Rev. B* **49**, 8024 (1994).
- [27] M. Shishkin, M. Marsman, and G. Kresse, *Phys. Rev. Lett.* **99**, 246403 (2007).
- [28] F. Bruneval, F. Sottile, V. Olevano, R. Del Sole, and L. Reining, *Phys. Rev. Lett.* **94**, 186402 (2005).
- [29] M. Rohlfing and S. G. Louie, *Phys. Rev. B* **62**, 4927 (2000).
- [30] P. Hohenberg and W. Kohn, *Phys. Rev.* **136**, B864 (1964).
- [31] W. Kohn and L. J. Sham, *Phys. Rev.* **140**, A1133 (1965).
- [32] A. L. Fetter and J. D. Walecka, *Quantum Theory of Many-particle Systems* (McGraw-Hill, San Francisco, 1971).
- [33] M. E. Casida, *Phys. Rev. A* **51**, 2005 (1995).
- [34] L. Hedin, *Phys. Rev.* **139**, A796 (1965).
- [35] G. Bussi, *Phys. Scr.* **2004**, 141 (2004).
- [36] G. Strinati, *Riv. Nuovo Cimento* **11**, 1 (1988).
- [37] J. P. Perdew, K. Burke, and M. Ernzerhof, *Phys. Rev. Lett.* **77**, 3865 (1996).
- [38] M. J. Oliveira and F. Nogueira, *Comput. Phys. Commun.* **178**, 524 (2008).
- [39] M. Fuchs and M. Scheffler, *Comput. Phys. Commun.* **119**, 67 (1999).
- [40] X. Gonze *et al.*, *Comput. Phys. Commun.* **180**, 2582 (2009).
- [41] X. Gonze, G.-M. Rignanese, M. Verstraete, J.-M. Beuken, Y. Pouillon, R. Caracas, F. Jollet, M. Torrent, G. Zerah, M. Mikami, P. Ghosez, M. Veithen, J.-Y. Raty, V. Olevano, F. Bruneval, L. Reining, R. Godby, G. Onida, D. Hamann, and D. Allan, *Z. Kristallogr.* **220**, 558 (2005).
- [42] X. Gonze, J.-M. Beuken, R. Caracas, F. Detraux, M. Fuchs, G.-M. Rignanese, L. Sindic, M. Verstraete, G. Zerah, F. Jollet, M. Torrent, A. Roy, M. Mikami, P. Ghosez, J.-Y. Raty, and D. Allan, *Comput. Mater. Sci.* **25**, 478 (2002).
- [43] D. J. Singh, *Planewaves, Pseudopotentials, and the LAPW Method* (Springer, New York, 2006).
- [44] <http://elk.sourceforge.net>
- [45] P. Giannozzi *et al.*, *J. Phys.: Condens. Matter* **21**, 395502 (2009).
- [46] J. Deslippe, G. Samsonidze, D. A. Strubbe, M. Jain, M. L. Cohen, and S. G. Louie, *Comput. Phys. Commun.* **183**, 1269 (2012).
- [47] R. W. Godby and R. J. Needs, *Phys. Rev. Lett.* **62**, 1169 (1989).
- [48] W. von der Linden and P. Horsch, *Phys. Rev. B* **37**, 8351 (1988).
- [49] G. E. Engel and B. Farid, *Phys. Rev. B* **47**, 15931 (1993).
- [50] R. Haydock, *Comput. Phys. Commun.* **20**, 11 (1980).

- [51] M. Rohlfing and S. G. Louie, *Phys. Rev. Lett.* **81**, 2312 (1998).
- [52] F. Fuchs, C. Rödl, A. Schleife, and F. Bechstedt, *Phys. Rev. B* **78**, 085103 (2008).
- [53] M. Dvorak, S.-H. Wei, and Z. Wu, *Phys. Rev. Lett.* **110**, 016402 (2013).
- [54] L. X. Benedict and E. L. Shirley, *Phys. Rev. B* **59**, 5441 (1999).
- [55] N. E. Christensen and I. Gorczyca, *Phys. Rev. B* **50**, 4397 (1994).
- [56] M. Grüning, A. Marini, and X. Gonze, *Nano Lett.* **9**, 2820 (2009).
- [57] A. Oschlies, R. W. Godby, and R. J. Needs, *Phys. Rev. B* **51**, 1527 (1995).